To What Extent Is Aeroelasticity Impacting Multi-Megawatt Wind Turbine Upscaling? A Critical Assessment

To What Extent Is Aeroelasticity Impacting Multi-Megawatt Wind Turbine Upscaling? A Critical Assessment

L. Pagamonci[1], F. Papi[1], F. Balduzzi[1], S. Xie[2], J. Sadique[2], P. Scienza[3], A. Bianchini[1,*]

[1] Dept. of Industrial Engineering, Università degli Studi di Firenze, Via di Santa Marta 3, 50139, Firenze, Italy

[2] Convergent Science Inc., 6400 Enterprise Ln, Madison WI 53719

[3] Convergent Science GmbH, Hauptstrasse 10, 4040 Linz, Austria

* alessandro.bianchini@unifi.it

Abstract. Aeroelasticity is recognized as the key enabler that allowed for the massive upscaling of wind turbines in the last decade, leading to long, slender, and flexible blades that equip rotors with lower specific power and unprecedented energy conversion capabilities. In this study, a selection of case studies with increasing size, specifically the NREL 5 MW, the DTU 10 MW, and the IEA 15 MW Reference Wind Turbines (RWTs) is considered to explore to what extent aeroelastic effects impact the functioning of these rotors. The rotors are not only different in size, with the 15 MW having blades nearly double the length of its 5 MW predecessor, but also in technological level as they belong to different phases of wind turbine development. To evaluate how these machines interact with complex inflow conditions, equivalent boundary conditions have been considered for all simulations, including a realistic atmospheric boundary layer, atmospheric turbulence, and wind shear. To carry out the comparative study, a new aero-servo-elastic module called CALMA is introduced herein, by coupling the engineering software OpenFAST with the CFD software CONVERGE, which solves the wind field and provides inflow conditions for the calculation of loads. Results show how not only aeroelasticity increasingly affects the power performance of the new-generation rotors, but is also a key driver of structural design, for example allowing for an alleviation of 1P load variations due to a sheared and turbulent inflow, thus proving that the inclusion of aeroelasticity in the design process is a key enabler to current and future upscaling trends.

1. Introduction

In the past decades wind turbine size has increased dramatically in a constant pursuit of lower Levelized Cost of Energy (LCOE) [1]. It is common knowledge, both in academia and industry, that this trend will continue in the coming years, with 14-15 MW offshore machines – with blades up to 120 meters long – currently being prototyped by the major manufacturers and 22 MW machines on the horizon as research turbines [2]–[4]. Due to their slender form factor, these cantilevered structures are designed to flex when aerodynamically loaded, resulting in deflections that can be in the order of tens of meters during operation. This structural behavior has a direct impact on blade aerodynamics, which in turn responds dynamically with unsteady forces acting on the blade. The global result is a mutual interaction between structure and aerodynamics, converging in the so-called aeroelastic response of the blade, which affects both its performance and structural stability. As blades get larger, the importance of aeroelasticity in their performance, aero-structural stability, loads, and safety is believed to increase by many experts [5]. Moreover, from a broader perspective, Blade Element Momentum Theory (BEMT) based models are still the industry workhorse when it comes to designing and certifying these machines. However, the validity of these models is increasingly questioned when large blade deflections may cause the rotor to interact with its own vorticity [5].

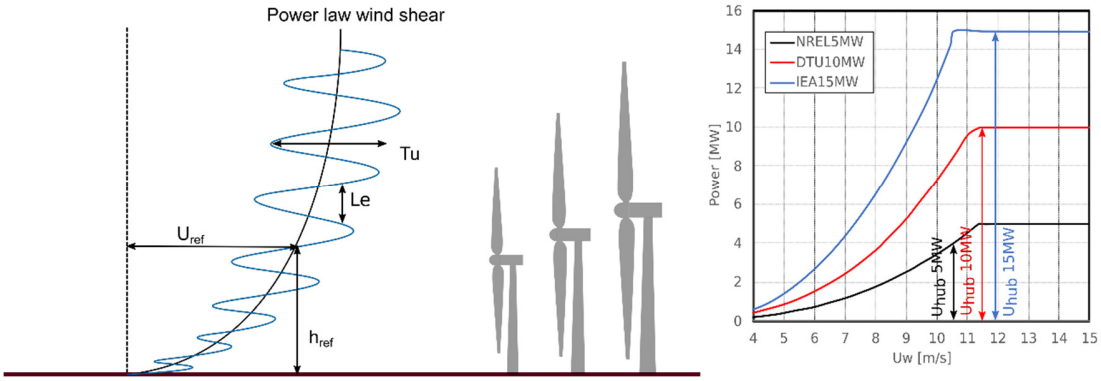

Figure 1 Inflow conditions adopted for the case study.

This study aims at being a contribution to the understanding of aeroelastic effects in the context of wind turbine upscaling by critically comparing a selection of case studies with increasing size, specifically the NREL 5 MW [6], DTU 10 MW [7] and IEA 15 MW [8] Reference Wind Turbines (RWTs), with the latter featuring blades that are nearly double the length of its 5 MW predecessor. Moreover, with the objective of evaluating how these machines respond to complex inflow conditions, the interaction of the different turbines with the ABL has also been studied by including atmospheric turbulence and wind shear in the simulations. As these test-cases reflect the trends and technology of their design period, we are here comparing not only rotors of different sizes, but also nearly more than a decade of technical innovation in turbine and blade technology. The new aero-servo-elastic tool CALMA (CONVERGE [9] Actuator Line Model for Aeroelasticity) is presented for the first time, and applied to the simulation of the three turbines. This tool has been developed by implementing the engineering code OpenFAST [10] inside the framework of the CONVERGE CFD software; the result of such coupling is a fully aero-servo-elastic Actuator Line Model (ALM), in which the two-way coupling between blade deformation and blades' aerodynamics can be properly resolved within the limitations of a blade-element-based approach. For a more realistic analysis, standard generator torque and blade pitch control is included in the analysis. The impact of aeroelasticity on rotor design and performance is critically analyzed and assessed by comparing rigid and flexible simulations for each RWT, focusing on both the rotor and the tower.

2. Study cases

Table 1 summarizes the main design and performance parameters for NREL 5 MW, DTU 10 MW and IEA 15 MW RWTs. Data for the 5 MW and the 15 MW have been downloaded from the respective GitHub repositories, while for the 10 MW they come from the work of [11]. For the current analysis, adaptions on the geometry of each tower from the offshore version were needed for the three turbines, so the transition piece has been eliminated and the tower has been extended to the ground level, maintaining a constant diameter.

The turbines are simulated while operating in an atmospheric boundary layer as shown in Figure 1, with an average wind velocity of 11 m/s at a reference height of 100 m and with a power law with exponent 0.2: these conditions make the DTU 10 MW and the IEA 15 MW operate in the above-rated conditions (with the 10 MW very close to rated), while the NREL 5 MW operates in below-rated conditions.

Table 1 Specifications of the three study cases.

Parameter	NREL 5 MW	DTU 10 MW	IEA 15 MW
Rated Power	5 MW	10 MW	15 MW
Rotor diameter	126 m	184 m	240 m
Hub radius	1.5 m	2.8 m	4.0 m
Cut-in/Cut-out wind speed	4 – 25 m/s	4 – 25 m/s	3 – 25 m/s
Rated wind speed	11.4 m/s	11.4 m/s	10.6 m/s
Rated rotor speed	12.1 rpm	9.6 rpm	7.55 rpm
Hub height	89.6 m	118.4 m	148.7 m
Rotor precone angle	-2.5°	-2.5°	-4
Rotor shaft angle	5°	5°	6°

3. Methods

The following section will present the coupling between OpenFAST and the CFD solver CONVERGE, as well as the methods for the generation of the correct inflow condition.

3.1. CALMA

The CALMA package, presented herein for the first time, comes from a coupling between the CFD solver CONVERGE and OpenFAST libraries, following the conceptual scheme of Figure 2. The concept is to re-create an ALM, similar to what originally developed by Shen et al. [12]. The coupling is achieved through the user-defined-function (UDF) API of CONVERGE.

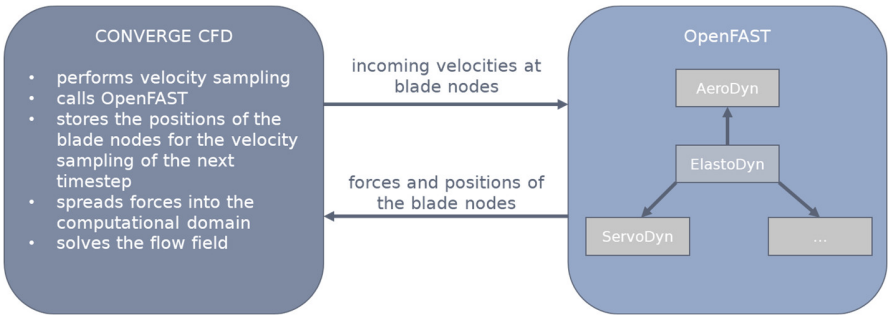

Figure 2 Working principle of CALMA.

CONVERGE acts as an inflow solver, determining the relative inflow velocity and angle of attack that are then used as inputs for OpenFAST, which solves the aerodynamics and the structure, and calculates the new positions of the ALM nodes. Aerodynamic forces and blade nodes position are then transferred back to CONVERGE. Forces are inserted into the flow field as volume sources, while nodes positions are used for the next ALM loop.

3.2. ALM setup

As shown by [13], the critical aspects when defining an Actuator Line are the number of sections, the velocity sampling, the airfoil polars, and the regularization kernel chosen for the force spreading. For the three turbines under consideration, the best setup is a tradeoff between the required discretization of blades and the mesh setup: for each blade, 40, 45 and 50 actuator points have been set for the NREL 5 MW, the DTU 10 MW and the IEA 15 MW, respectively. In addition, an actuator line for the towers has been also included, featuring the same number of sections of the respective blade.

To properly sample the inflow velocity data from the flow domain at the actuator points along the line, the line average velocity sampling approach [14] has been chosen, with six sampling points for each section.

3.3. OpenFAST setup

The entire framework of OpenFAST is accessible on runtime in CALMA. For this specific application, AeroDyn, ElastoDyn, and ServoDyn modules have been activated, with the CFD acting as an external solver for the inflow conditions at each timestep, similarly to an external InflowWind module.

The aerodynamics of the blades (for which airfoil polars have been directly downloaded from the respective GitHub repositories of each institute) and tower are solved inside AeroDyn, passed to the CFD solver and then properly spread inside the flow field via a distribution function. The Beddoes-Leishman dynamic stall model [15] has been employed for both the rigid and the flexible cases. Structural dynamics are solved with the modal-based approach of ElastoDyn. More precisely, the deformations of the blades and the tower are computed as the modal superposition of the first two fore-aft and side-side modes for the tower, and the first two flapwise and the first edgewise modes for the blades. It must be noted that torsions are not solved inside ElastoDyn. This is a flaw for a full aeroelastic analysis and will be hopefully fixed in the near future by including BeamDyn in the workflow.

Industry standard blade pitch and generator torque control are included in the analysis. This is seen by the authors as a key novelty of the study. To ensure a fair comparison, all three turbines are controlled with the

ROSCO controller version 2.4.1 [16]. The choice has fallen on this controller as it is open-source, and being developed by NREL, input files with specific tunings for the NREL 5 MW and IEA 15 MW test cases are publicly available. The controller parameters and gain scheduling parameters publicly available with the Rosco v2.5 release are used as-are for the IEA 15 MW. For the NREL 5 MW on the other hand, preliminary step-tests showed erratic pitch behaviour. The ROSCO controller uses a Proportional-Integral (P-I) strategy to control rotor speed through blade pitch variations. Because the response of the system is non-linear, a gain scheduling table is used, where rather than being constant, proportional (K_i) and integral (K_p) gains are assigned based on the instantaneous blade pitch angle. To mitigate the erratic behaviour, the magnitude of the proportional and integral gains was manually reduced, especially at low blade pitch angles. For the DTU 10 MW RWT no input file for the ROSCO controller is publicly available. Therefore, the semi-automatic tuning routine that is available with the controller [16]–[18] was exploited. For the pitch controller, the tuning strategy is based on a user-defined choice of natural frequency and damping ratio, through which K_i and K_p are assigned. In an attempt to minimize rotor speed overshoot, a fairly high value of damping ratio of 1 is chosen. For the natural frequency however, a lower natural frequency of 0.15 rad/s produced more stable behaviour at lower pitch angles, while a higher natural frequency of 0.35 rad/s was necessary at higher blade pitch angles to effectively control the rotor speed. Therefore, the outcomes of the two tuning strategies are combined trough cubic splines: the proportional and integral gains coming from a high natural frequency are used at high pitch angles, and those coming from a lower gain are used at lower pitch angles. The outcomes of the controller tuning are shown in Figure 3, where the time histories of rotor speed (controlled variable) and blade pitch (controlling variable) are shown during a step test from 9 m/s to 25 m/s in 2 m/s increments in OpenFAST. Although some oscillations in both blade pitch and rotor speed are shown in the IEA 15 MW and NREL 5 MW models at lower pitch angles and rotor speeds, rotor speed is well controlled in all three test cases. The controller showed good regulation capabilities even in a step-down test, not shown herein for brevity. As for the torque controller, the classical K-ω^2 law is used below rated. Above rated torque is kept constant in all three test cases.

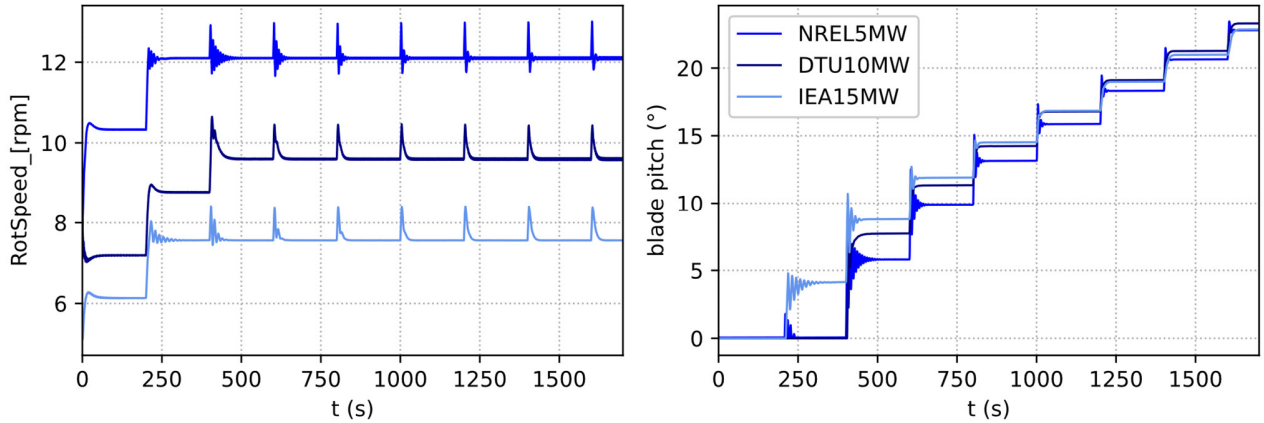

Figure 3 Rotor speed and blade pitch during a step test. Wind speed from 9m/s to 25m/s in 2m/s increments.

3.4. CFD solver settings and simulation setup

For an effective comparison of the three machines, a common setup has been chosen, with few modifications from turbine to turbine, mainly to account for accuracy requirements (e.g., the computational grid). The incompressible turbulence flow is modeled by means of an unsteady Reynolds-Averaged Navier-Stokes (URANS) approach.

The Reynolds stress tensor is modeled by the Standard k-ε model. An orthogonal Cartesian grid based on an automated cut-cell algorithm is used (see Figure 4), having the largest cell size of 25.2 m (i.e., 0.2 D referring to the NREL 5 MW), and progressively refining near the rotor and on the wake, reaching the smallest mesh size of 1.575 m around the rotor blades. A 3780x2520x1260 m computational domain envelops the simulated flow field, with the inlet at a distance of 1260 m from all the turbines. This choice ensures coherence between the simulated testcases and allows for the same turbulence conditions for all three rotors, as explained in more details in Section 3.5.

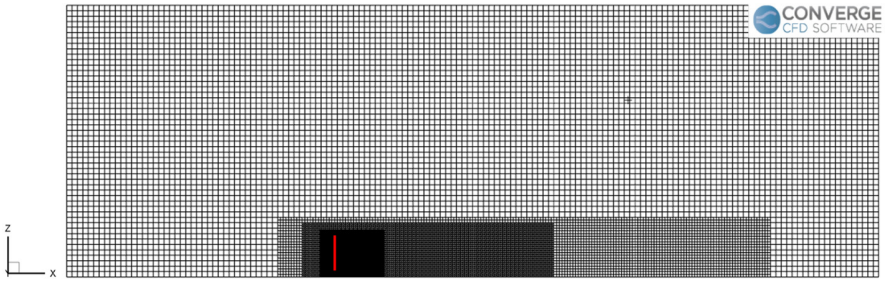

Figure 4 Computational domain and mesh. Rotor position in red color.

3.5. TuRBUiND

Along with the creation of a proper wind profile as inflow conditions, the reproduction of a realistic ABL also requires an unsteady, random macroturbulence inside the flow field. While the mean wind shear conditions were already available within CONVERGE [19], the instantaneous turbulence structure is here generated by TuRBUiND (Turbulence Random Boundary U-velocity Inlet Normal Distribution), a model developed by Balduzzi et al. [20], at the inlet boundary of the computational domain to allow reproducing realistic atmospheric turbulence structures also in URANS simulations. The basic idea of the original model is the insertion of macroturbulence in the domain by means of a random distribution of velocity perturbations at the velocity inlet. To do so, random velocity fluctuations are computed and summed with the mean wind shear to define the inlet velocity profile. This is inserted into the inlet boundary by looping at each face cell center. The intensity of the fluctuations is controlled by a Gaussian probability distribution, whose standard deviation and mean value are controlled by the user. The update of the inlet velocity profile follows a user-defined timing, both for the periodical generation of new profiles and for the gradual profile update from the older to the new one, called blending period. To summarize, the parameters that regulate the generation of the turbulence are the following:

- *Inlet elements size* – As a consequence of looping at all inlet face cell centers, the size of the elements at the inlet boundary is linked closely to the characteristic *Le* (length scale, Figure 1) of the generated turbulence: the larger the elements, the greater the length scale. The inlet mesh size can then be adjusted with proper sensitivity analyses at the beginning of the simulations, as shown in the next paragraph.
- *Profile update frequency* – The update frequency of the inlet velocity profile must be chosen before its assignment at the inlet boundary, as it will remain constant for the whole simulation. Together with the previous parameter, it plays a fundamental role for the *Le* of the turbulent flow. Indeed, higher frequencies will produce smaller length scales. It is important to notice that the length scale of the turbulent flow is related only to the physical time between two consecutive updates, but it is independent from the simulation time step, so this can be chosen conveniently, whether fixed or variable. For this work, however, a fixed time step has been set, as required by OpenFAST in the current implementation status.
- *Standard deviation of random number generator* – The standard deviation of the Gaussian distribution followed by the random number generator has a direct influence on the *Tu* (Figure 1), defined as in Eq. 1, with U_{rms} the root mean square deviation of the fluctuating velocity around the mean value U_{mean}. As already noticed by the authors, turbulence grows with the standard deviation even if not in a linear way, especially along the domain and at the turbine location, requiring consideration of turbulence decay during the case setup.

$$Tu = \frac{U_{rms}}{U_{mean}} \quad (1)$$

A preliminary calibration has been thus performed in an empty domain, in order to have representative values of *Tu* and *Le* at the turbine position, and to generate a common initialized flow field for all the simulated turbines. A qualitative overview of the resulting flow field can be observed in Figure 5. Upon analysis of Figure 6, it can be noticed that, by imposing a standard deviation equal to 8.0, 8 seconds of update period, 4 seconds of blending period and a mesh grid size equal to 25.2 m, a $Tu \approx 9\%$ and a $Le \approx 45$m were obtained at the hub position. The values of *Tu* and *Le* have been calculated following the procedure proposed by [21]. Considering the turbulence decay, the distance of the three rotors from the inlet has been imposed constant, in order to guarantee the similarity of the simulated testcases. Finally, it must be specified that also the wind shear has been included, with 11 m/s of mean velocity at hub (chosen at the height of 100 m) and a power law with exponent 0.2.

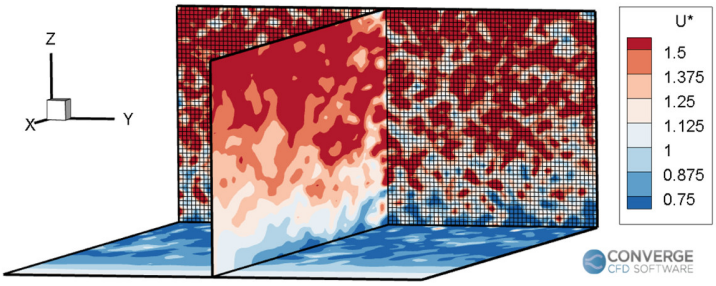

Figure 5 Flow field from the calibration. Inlet boundary in the background. $U^{*}=U/U_{mean}$, with U_{mean}=11 m/s.

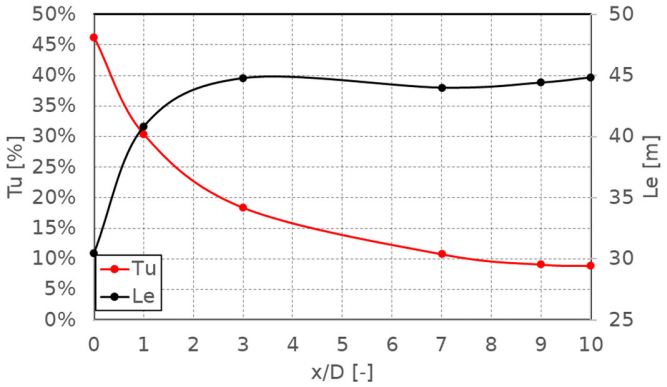

Figure 6 Tu and Le trends along the domain; D=126 m (NREL 5 MW).

4. Results

4.1. Steady-state and uniform conditions

The effectiveness of the CALMA approach in reproducing the attended performance of the three study cases was first checked by comparing for example the results of the NREL 5 MW turbine operating in steady-state and uniform inflow conditions with the ones from the official report [6], reported in Figure 7 (left). Overall, sound agreement was found in comparison with the expected performance along the entire operating curve, especially in the below-rated and rated/above-rated conditions, with some slight differences in the calculated rotor thrust in the near-rated conditions. Focusing on the structural response (Figure 7 (right)), only a slight overestimation of the out-of-plane deflection in the near-rated conditions, mainly as a consequence of the discussed overestimation of the rotor thrust.

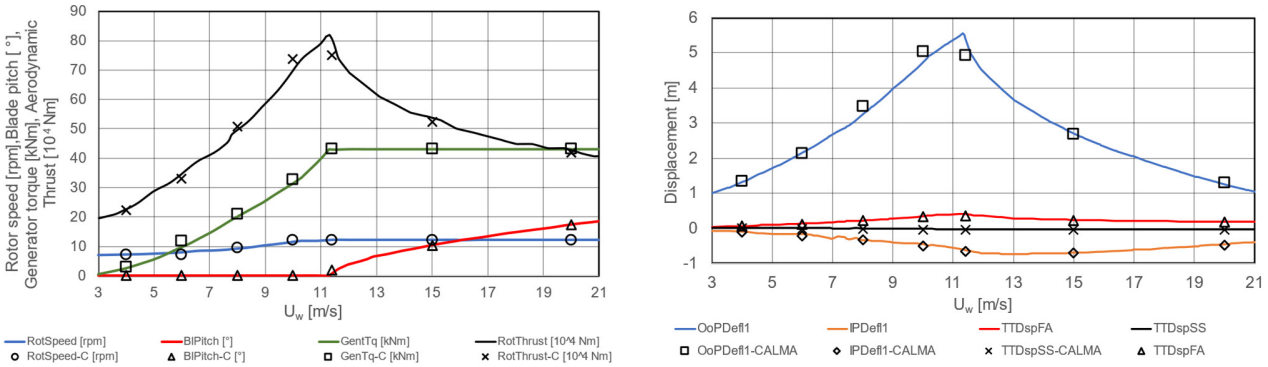

Figure 7 (left) CALMA results compared to the ones from NREL 5 MW technical report; **(right)** Main deflections of the structure: following the legend from left to right, out-of-plane and in-plane deflections of blade 1, fore-aft and side-side deflections of the tower top.

4.2. Sheared and turbulent inflow

Figure 8 reports an overview of the flow field at three different heights probed one diameter and three diameters upstream the rotor, referring to the IEA 15 MW simulations. The rigid and flexible cases are compared in order to check the proper reconstruction of the wind shear conditions far enough from the rotor and the similarity, in the time domain, between the flow conditions approaching the rigid and flexible rotors. Good similarity can be noticed, with a difference in the average axial wind speed of around 1%, at the hub height (150 m). This slight difference is related to the different rotor response to the incoming inflow.

Focusing now on averaged performance metrics, Table 2 reports an overview of the most relevant ones for all three turbines. If one compares the DTU 10 MW and the IEA 15 MW, no substantial differences can be noticed in terms of final power output between the rigid and the flexible cases. This is to be expected as the two machines operate above rated wind speed, and the controller is able to compensate for aerodynamic power variation by adjusting the blade pitch. Increases in rotor thrust are therefore experienced. Different considerations must be done for the NREL 5 MW. As shown in Table 2, for this case the thrust is almost constant, but the aerodynamic power decreases. An explanation for this trend can be found by inspecting the time series of the blade pitch in Figure 9: under the imposed wind inflow conditions, this turbine is operating over the knee of the power curve, with the controller changing the blade pitch only in restricted time intervals, corresponding to the above rated conditions. The higher is the total time in which the turbine is working in that region, the higher is the final average value of torque. As can be noticed in the figure, the rigid turbine is the one that is working in the above rated conditions for most of the time, so a higher value of average power can be expected.

Interesting findings can be also highlighted by analyzing the span-wise values of axial and tangential forces (with respect to the rotor plane), as reported in Figure 10. Focusing first on tangential forces, it can be noticed how for the DTU 10 MW and the IEA 15 MW, both working in above rated region, the controller keeps the torque constant by reducing the blade pitch. This leads to a change in operating conditions and to an inward shift of the tangential force. Such a shift is also noticeable for the IEA 15 MW in the normal force, although this metric is higher along the entire blade span when aeroelastic effects are included in the analysis. Similar considerations can be drawn for the DTU 10 MW, where the increase in normal force is even higher with respect to the rigid case.

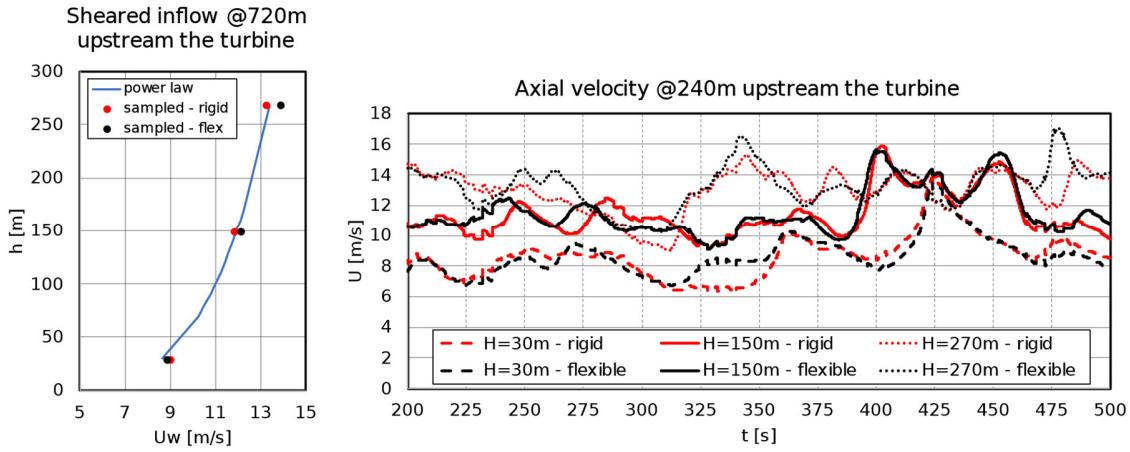

Figure 8 Incoming flow field in front of the rotor for the two cases of the IEA 15 MW; left: average wind speed, comparisons with theoretical power law; right: timeseries trend.

Table 2 Aggregate performance metrics.

Parameter	**NREL 5 MW**			**DTU 10 MW**			**IEA 15 MW**		
Case	Rigid	Flexible	Δ	Rigid	Flexible	Δ	Rigid	Flexible	Δ
Aerodynamic Thrust [kN]	677.5	676.4	-0.2%	1257.2	1322.9	5.2%	1695.1	1738.3	2.5%
Generator Power [MW]	4.53	4.39	-3.1%	9.38	9.38	0.0%	15.05	15.09	0.3%
Blade pitch [°]	0.92	0.60	-0.32	4.09	3.51	-0.58	6.24	6.10	-0.14
Rotor speed [rpm]	12.00	11.98	-0.2%	9.58	9.57	-0.1%	7.56	7.56	0.0%

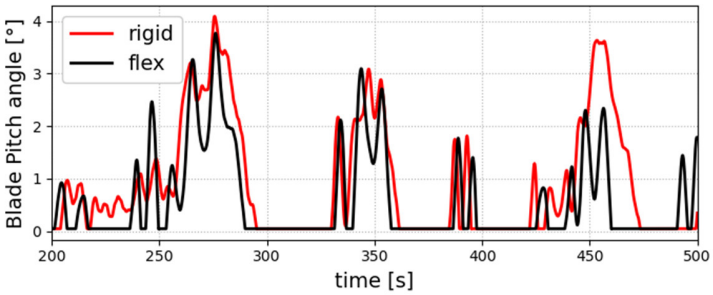

Figure 9 Blade pitch trend of the NREL 5 MW simulations, comparisons between rigid and flexible case.

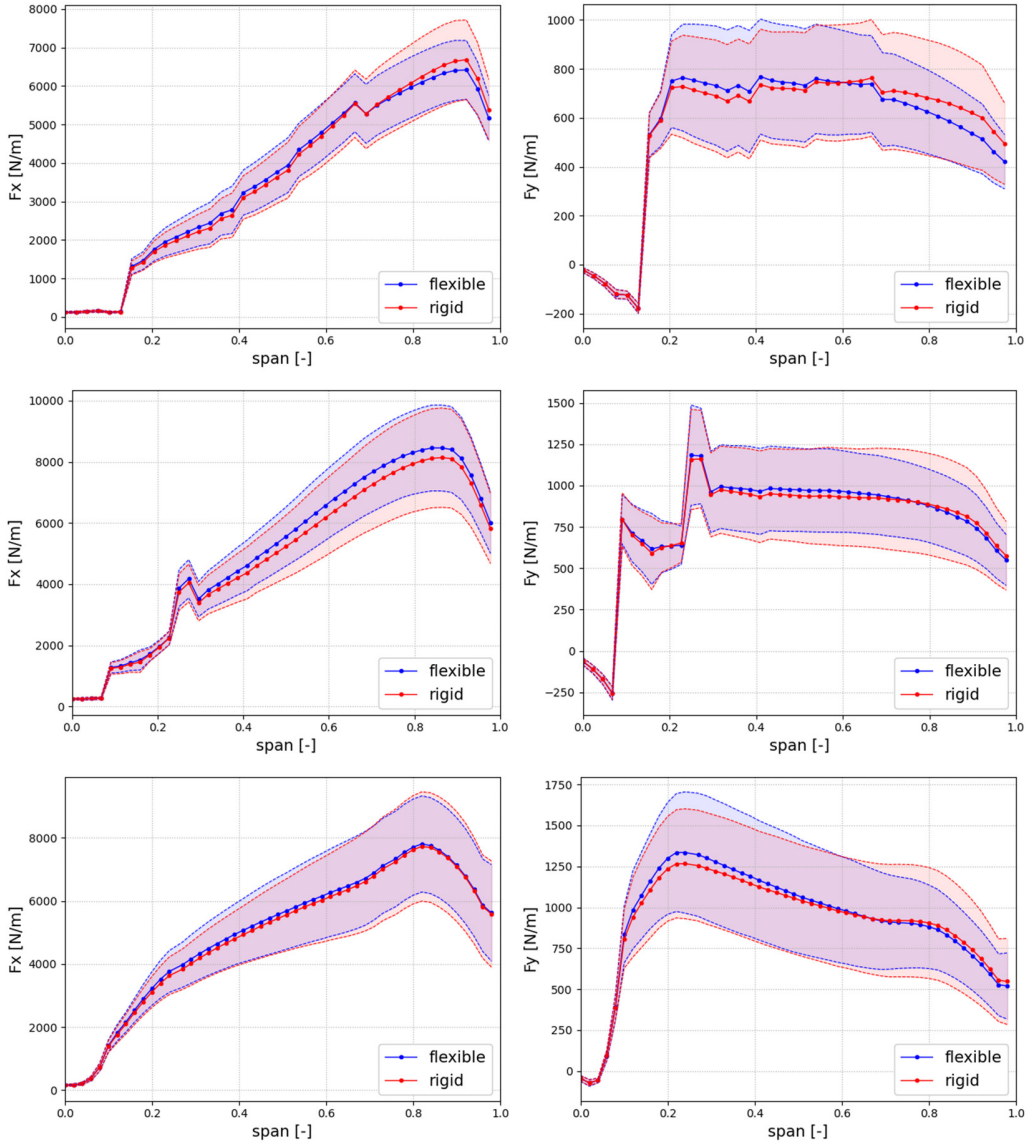

Figure 10 From top: span-wise values of forces in the normal (x) and tangential (y) direction, with respect to the rotor plane, of the NREL 5 MW, DTU 10 MW and IEA 15 MW; line: mean values; shaded: standard deviation of the time-series data.

An important proof of the impact of aeroelasticity can be seen in Figure 11, in which the time-series and the Power Spectral Density (PSD) of the aerodynamic torque is plotted for the NREL 5 MW and the IEA 15 MW, respectively. It can be noticed how, moving to larger rotors, higher 3P (three times per revolution) components show up, especially in the rigid simulations. This result implies that the increased flexibility of new-generation rotors filters most of the high frequency inflow variations arising during operation in a sheared and turbulent flow field. Indeed, one could observe how the trend of the axial structural velocity (Figure 12) of the blade is beneficial for the alleviation of 1P (one time per revolution) fluctuations: in fact, a negative structural velocity means a higher apparent wind, and therefore higher relative speed and aerodynamic force, while a positive structural velocity leads to a lower aerodynamic force. As shown in Figure 12, the structural velocity is mostly negative when the blade is pointing downwards (90°-270°) and positive when it is pointing upwards, partially compensating for the variation in relative inflow caused by wind shear. Furthermore, this effect is more pronounced on the IEA 15 MW. Such an outcome is of particular relevance also during the structural design of the blades, as it affects design choices both in terms of maximum loading and resistance to fatigue.

Moving to the structural analysis of the turbines, one of the main elements of interest is the elastic response of the blades, both in spanwise average terms, and in time and frequency domains. The main results of this analysis are summarised in Figure 13, which shows the evolution of the flapwise deflections for blade 1. On the left-hand side, the spanwise average values along the blade span are plotted, with deflections referred to the respective blade radius. Despite the differences in geometry and performance, analogous behaviour can be noticed for NREL 5 MW and the DTU 10 MW.

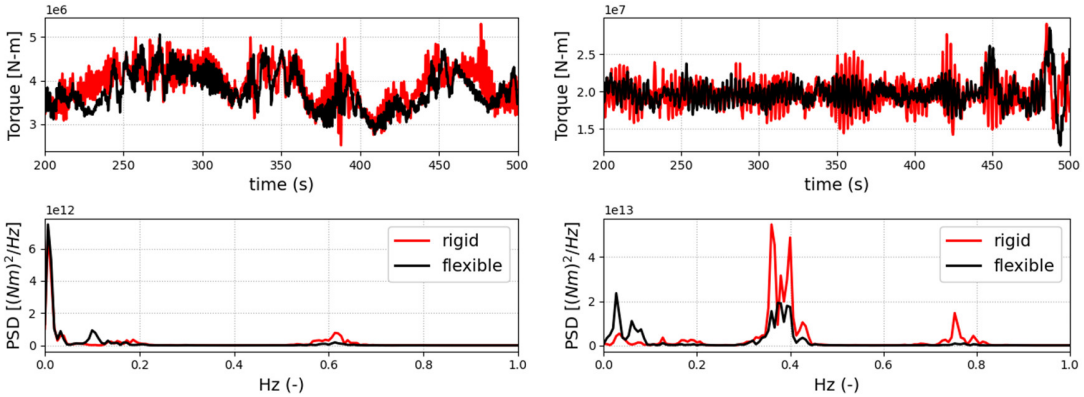

Figure 11 Time series data and PSD analysis of the aerodynamic torque, comparisons between NREL 5 MW (left) and IEA 15 MW (right).

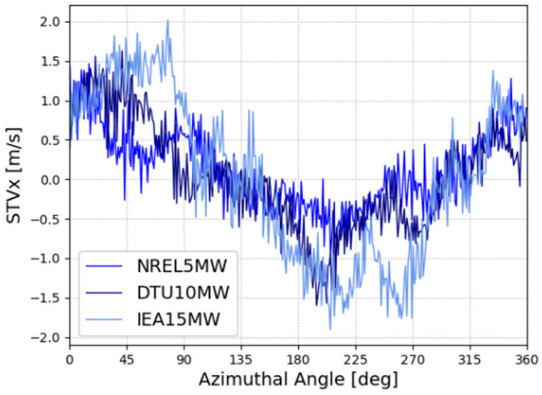

Figure 12 Azimuthally averaged structural velocity in the axial direction. The azimuthal average is computed dividing the rotor revolution into 1° bins and computing the mean of recoded values within each bin.

On the other hand, the IEA 15 MW shows slightly higher deflections for most of the blade span, both in terms of mean value and in the standard deviation, meaning that the maximum values of the deflections are generally higher, thus highlighting a larger impact of aeroelasticity.

This conclusion is also proved by the time-series trend and the PSD analysis of tip deflections for blade 1 (Figure 13), where both higher absolute values and frequency responses can be noticed for the IEA 15 MW. It is important to note that, as stated previously, blade torsion was not included in this analysis. This effect could be significant on a large blade such as the one mounted to the IEA 15 MW and could bring the result more in line with smaller rotors. Regarding the frequency response, it is worth noticing that the most important peak (Figure 13) is at 1P: this is the frequency of the passage of the blade in front of the tower, but also a significant frequency for wind shear loads on the blades. A general interpretation of this relies on the combination of two important elements of this work: blade aeroelastic design and sheared turbulent inflow conditions. As discussed, the upscaling of the rotors leads to slender and longer blades, which experience a greater variability in inflow conditions through one revolution. Despite the large deflections in the case of the larger machine (Figure 13 right), relative deflection and standard deviations are similar in all three cases (Figure 13 right). The effects of the increase in blade size are more evident if considering the trend of the axial structural velocity along the blade span (Figure 14), where the IEA 15 MW clearly shows the highest variations.

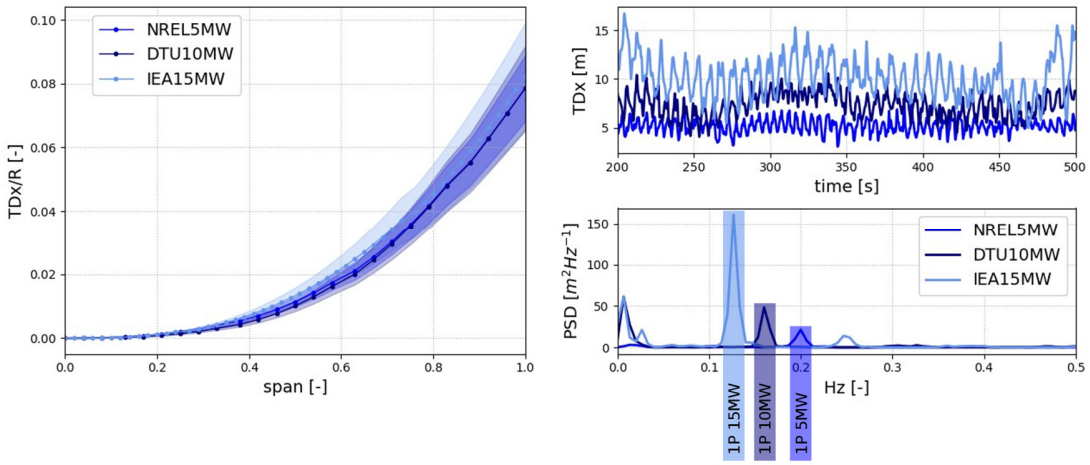

Figure 13 Left: spanwise values of out-of-plane deflections for blade 1 normalized with respect to blade length, line – average value, shaded – standard deviation of the data. Right: timeseries data and PSD of blade tip displacements.

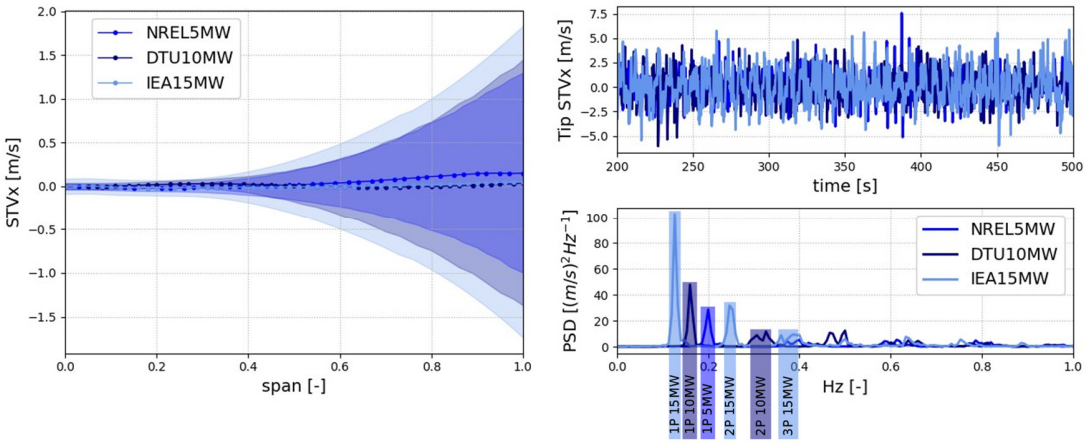

Figure 14 Structural axial velocity; left: mean values (lines) and standard deviation of the time series data; right: time series data and PSD analysis of the tip axial structural velocity.

From a perusal of the PSD, a prominent peak at 1P can be noted, effectively indicating that aeroelastic effects dampen the 1P variation in inflow velocity due to wind shear.

Finally, focusing on the turbine towers (Figure 15), it can be noticed how the IEA 15 MW shows the lowest tower displacements, while the DTU 10 MW and the NREL 5 MW show the highest tower top displacements in the fore-aft direction and in the side-to-side direction respectively. This is in line with the fact that the IEA 15MW tower is stiffer, and deflects less despite the increased aerodynamic thrust with respect to the other designs. This may be explained by the fact that tower designs are typically frequency and fatigue constrained rather than stress constrained. Therefore, a less efficient use of the material may be required to place the natural frequencies in the appropriate range. Thus, as demonstrated in Figure 15, a higher tower may not always be more flexible than a lower one. Passing to the frequency domain instead, the higher peaks come from the 15 MW, especially for the fore-aft deflections, where a 3P peak takes place.

It is worth noting that this peak only takes place for the 15 MW, and one of the reasons relies once again on the dynamic response of the system: as blade deflections have both a higher mean value and a stronger fluctuating component, the structural response of the tower are influenced by these fluctuations. As for side-side displacements, a strong peak at 2P can be seen for the IEA 15 MW. For this test case, the 2P frequency is close to the tower natural frequency. In absence of aerodynamic damping, as in case of side-side deflections, this excites the first tower side-side mode, resulting in the observed behaviour.

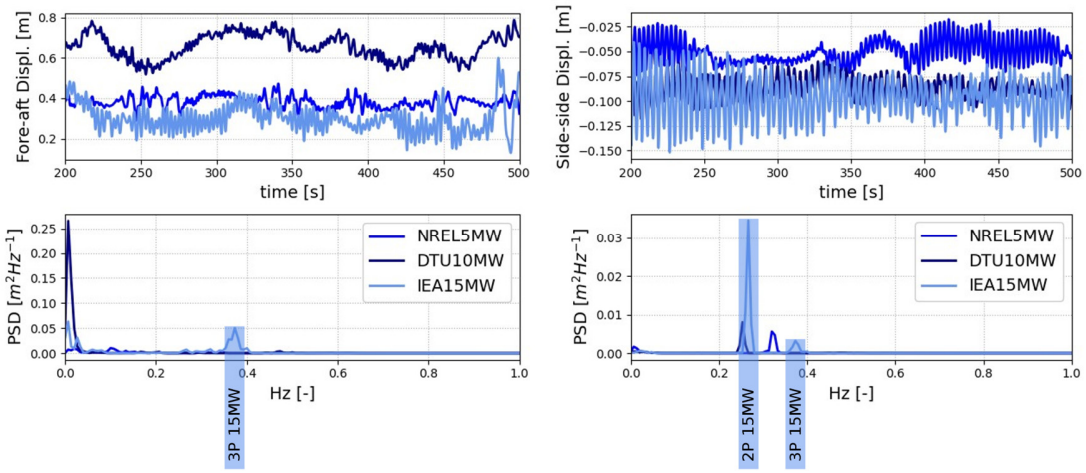

Figure 15 Tower displacements; top: time-series data; below: PSD analysis.

5. Conclusions

The study focuses on the analysis of the relative impact of aeroelastic effects in modern multi-megawatt turbines of increasing size operating in realistic ABL and turbulence. To this end, the new ALM tool CALMA, coupling OpenFAST with CONVERGE CFD solver, is used together with the turbulence generator TuRBUiND, specifically thought for use in a URANS framework.

Analysing the average values, differences between the rigid and flexible simulations are evident in the rotor mean performance, with a general underestimation of the rotor thrust between 2.5% and 5%, in conditions of constant power generation and if operating slightly above the rated conditions, as seen for the DTU 10 MW and the IEA 15 MW. For the NREL 5 MW, operating over the knee of the power curve, the aerodynamic thrust is almost constant and the generated power decreases in response to the blade pitch regulation. Differences can be noticed also by comparing the distribution of forces along the blade span. In the case of the IEA 15 MW and DTU 10 MW, which are operating slightly above rated, the inclusion of aeroelasticity changes the operating point as the controller compensates for the higher aerodynamic power. Consequently, the tangential force shifts towards the rotor hub and the thrust force increases.

The IEA 15 MW turbine in particular showed strong 1P load variation on the blades in rigid conditions. This is due to the greater variability in wind speed that this larger rotor is subject to due to wind shear. The inclusion of blade flexibility acts like a filter, partially dampening out the 1P load variations, proving that considering the aeroelasticity in the design process of these machines is a key enabler to current and future upscaling trends.

In conclusion, this work represents a first contribution in the understanding of the impact of aeroelasticity on wind turbine upscaling. Future refinements could include the analysis of more operating conditions and the inclusion of blade torsional flexibility, to fully understand the implications of aeroelastic tailoring in modern wind turbine rotors.

Data Availability

All the figures and the controller input files are available upon request.

Author Contributions

L. Pagamonci created the tool that is used in these analyses, performed all the simulations, interpreted the results, and wrote the first draft. F. Papi helped conceptualize the study, performed the control algorithm tuning, contributed to post-processing and interpretation of the result. F. Balduzzi and A. Bianchini developed the TuRBUiND synthetic inflow turbulence generator, helped conceptualizing the study, and interpreting results; A. Bianchini and F. Papi supervised the research project. S. Xie, J. Sadique, P. Scienza supported the development of CALMA and supervised the project. All authors contributed to the editing and revising the manuscript.

References

[1] P. Veers *et al.*, "Grand Challenges in the Design, Manufacture, and Operation of Future Wind Turbine Systems," *Wind Energy Sci. Discuss.*, vol. 2022, pp. 1–102, 2022, doi: 10.5194/wes-2022-32.
[2] "IEA-22-280-RWT." IEAWindTask37, May 17, 2023. Accessed: May 29, 2023. [Online]. Available: https://github.com/IEAWindTask37/IEA-22-280-RWT
[3] "V236-15.0 MW™," May 26, 2023. https://www.vestas.com/en/products/offshore/V236-15MW (accessed May 29, 2023).
[4] "Offshore Wind Turbine SG 14-222 DD I Siemens Gamesa." https://www.siemensgamesa.com/products-and-services/offshore/wind-turbine-sg-14-222-dd (accessed May 29, 2023).
[5] P. Veers *et al.*, "Grand challenges in the science of wind energy," *Science*, Oct. 2019, doi: 10.1126/science.aau2027.
[6] J. Jonkman, S. Butterfield, W. Musial, and G. Scott, "Definition of a 5-MW Reference Wind Turbine for Offshore System Development," NREL/TP-500-38060, 947422, Feb. 2009. doi: 10.2172/947422.
[7] C. Bak *et al.*, "The DTU 10-MW reference wind turbine," presented at the Danish wind power research 2013, 2013.
[8] E. Gaertner *et al.*, "IEA Wind TCP Task 37: Definition of the IEA 15-Megawatt Offshore Reference Wind Turbine," National Renewable Energy Lab. (NREL), Golden, CO (United States), NREL/TP-5000-75698, Mar. 2020. doi: 10.2172/1603478.
[9] "Richards K.J., Senecal, P.K., and Pomraning, E., CONVERGE 3.0, Convergent Science, Madison, WI (2023)."
[10] National Renewable Energy Laboratory, "OpenFAST," *GitHub*. https://github.com/OpenFAST (accessed Oct. 31, 2019).
[11] S. Perez-Becker, F. Papi, J. Saverin, D. Marten, A. Bianchini, and C. Paschereit, *Is the Blade Element Momentum Theory overestimating Wind Turbine Loads? – A Comparison with a Lifting Line Free Vortex Wake Method*. 2019. doi: 10.5194/wes-2019-70.
[12] J. N. Sørensen and W. Z. Shen, "Numerical Modeling of Wind Turbine Wakes," *J. Fluids Eng.*, vol. 124, no. 2, pp. 393–399, Jun. 2002, doi: 10.1115/1.1471361.
[13] N. Troldborg, "Actuator line modeling of wind turbine wakes," 2009.
[14] E. Jost, L. Klein, H. Leipprand, T. Lutz, and E. Krämer, "Extracting the angle of attack on rotor blades from CFD simulations," *Wind Energy*, vol. 21, no. 10, pp. 807–822, Oct. 2018, doi: 10.1002/we.2196.
[15] K. G. Pierce, "Wind turbine load prediction using the Beddoes-Leishman model for unsteady aerodynamics and dynamic stall," 1996.
[16] N. J. Abbas, D. S. Zalkind, L. Pao, and A. Wright, "A reference open-source controller for fixed and floating offshore wind turbines," *Wind Energy Sci.*, vol. 7, no. 1, pp. 53–73, Jan. 2022, doi: 10.5194/wes-7-53-2022.

[17] "ROSCO Toolbox. Version 1.0.0," GitHub, 2020. [Online]. Available: https://github.com/NREL/rosco_toolbox
[18] N. J. Abbas, A. D. Wright, and L. Pao, "An Update to the NREL Baseline Wind Turbine Controller: Preprint," National Renewable Energy Lab. (NREL), Golden, CO (United States), NREL/CP-5000-75433, Feb. 2020. Accessed: Oct. 18, 2022. [Online]. Available: https://www.osti.gov/biblio/1601147
[19] S. Xie and J. Sadique, "CFD Simulations of Two Tandem Semi-Submersible Floating Offshore Wind Turbines Using a Fully-Coupled Fluid-Structure-Interaction Simulation Methodology," in *IOWTC2022*, ASME 2022 4th International Offshore Wind Technical Conference, Dec. 2022. doi: 10.1115/IOWTC2022-98645.
[20] F. Balduzzi, M. Zini, G. Ferrara, and A. Bianchini, "Development of a Computational Fluid Dynamics Methodology to Reproduce the Effects of Macroturbulence on Wind Turbines and Its Application to the Particular Case of a VAWT," *J. Eng. Gas Turbines Power*, vol. 141, no. 111010, Oct. 2019, doi: 10.1115/1.4044231.
[21] L. A. El-Gabry, D. R. Thurman, and P. E. Poinsatte, "Procedure for determining turbulence length scales using hotwire anemometry," 2014.